

# Comparison of experimental data and three-dimensional simulations of ion beam neutralization from the Neutralized Transport Experiment

C. Thoma and D. R. Welch

*ATK Mission Research, Albuquerque, New Mexico 87110*

S. S. Yu, E. Henestroza, P. K. Roy, and S. Eylon

*Lawrence Berkeley National Laboratory Berkeley, Berkeley California 94720*

E. P. Gilson

*Princeton Plasma Physics Laboratory, Princeton, New Jersey 08543*

(Received 30 September 2004; accepted 8 December 2004; published online 14 March 2005)

The Neutralized Transport Experiment at Lawrence Berkeley National Laboratory has been designed to study the final focus and neutralization of high perveance ion beams [E. Henestroza, S. Eylon, P. Roy, S. Yu, A. Anders, F. Bieniosek, W. Greenway, B. Logan, R. MacGill, D. Shuman *et al.*, *Phys. Rev. ST-Accel. Beams* **7**, 083501 (2004)]. Preformed plasmas in the last meter before the target of the scaled experiment provide a source of electrons which neutralize the ion current and prevent the space-charge-induced spreading of the beam spot. Neutralized Transport Experiment physics issues are discussed and experimental data are analyzed and compared with three-dimensional (3D) particle-in-cell simulations. Along with detailed target images, 4D phase-space data at the entrance of the neutralization region have been acquired. These data are used to provide a more accurate beam distribution with which to initialize the simulation. Previous treatments have used various idealized beam distributions which lack the detailed features of the experimental ion beam images. Simulation results are compared with experimental measurements for  $K^+$  ion beams ( $\sim 250$  keV) with dimensionless perveance of  $(1-7) \times 10^{-4}$ . In both simulation and experiment, the deduced beam charge neutralization is encouraging for heavy ion fusion and high energy density physics applications. © 2005 American Institute of Physics. [DOI: 10.1063/1.1854174]

## I. INTRODUCTION

In the neutralized ballistic transport (NBT) scheme<sup>1-8</sup> for heavy ion fusion (HIF), intense ion beams drift for several meters after the final focus magnet through the reactor chamber to an inertial confinement fusion (ICF) target.<sup>9</sup> Another application for NBT is to focus heavy ion beams onto targets for high energy density physics (HEDP) experiments. A recent HIF design (Robust Point Design<sup>10</sup>) and a proposed HEDP experiment<sup>11</sup> both require 1-5 mm spot sizes. For high perveance beams, in which the space charge tends to blow up the spot size, this focusing requires significant neutralization of the beam space charge.<sup>12</sup> The Neutralized Transport Experiment (NTX) at Lawrence Berkeley National Laboratory<sup>13-15</sup> has been designed to study the final focus and neutralization of high perveance ion beams and to validate theoretical and simulation models<sup>15</sup> for driver scale transport.

An analytic estimate<sup>12</sup> places an upper limit on beam perveance for vacuum ballistic transport to millimeter spot sizes of  $K \sim 10^{-5}$ . Perveance, a dimensionless quantity somewhat loosely defined as the ratio of the beam potential to kinetic energy, is given in cgs units by

$$K = \frac{2eZI_b}{\beta_b^3 \gamma_b^3 c^3 m_b},$$

where  $I_b$  is the (singly stripped) ion beam current. Also  $Z, \beta_b c, m_b,$  and  $\gamma_b$  are the beam charge state, velocity, mass,

and relativistic factor, respectively. The robust point design study has found it advantageous to operate at beam perveance values of up to several times  $10^{-4}$ , well above the vacuum transport cutoff. For such high perveance beams additional neutralization is required.

Since both the beam envelope and neutralization scale primarily with perveance,<sup>16</sup> it is possible to scale the experiment to lower mass ions and particle energy as well as physical size while still preserving transverse dynamics<sup>17</sup> and neutralization physics. Several driver scale issues cannot be addressed in a small experiment. Most notably, since cross sections for processes such as beam stripping and collisional ionization of background gas are strongly dependent on energy, collisional processes cannot be modeled on a small scale. The effects of multiple beams, in which the perveance may increase with the number beams in the region of overlap, obviously cannot be considered by a single beam experiment such as NTX. High current effects, such as magnetic pinching and filamentation of the beam, are not significant at the low current levels of NTX, but could be significant at the driver scale for HIF. Although some preliminary simulation work has been done on beam interactions and high current effects,<sup>18</sup> future experiments on a larger scale than NTX are needed to assess their effects.

In the NTX experiment, a low emittance  $K^+$  ion beam is focused outside the neutralization region and passes through a 10 cm long Al plasma produced by a pulsed cathode arc

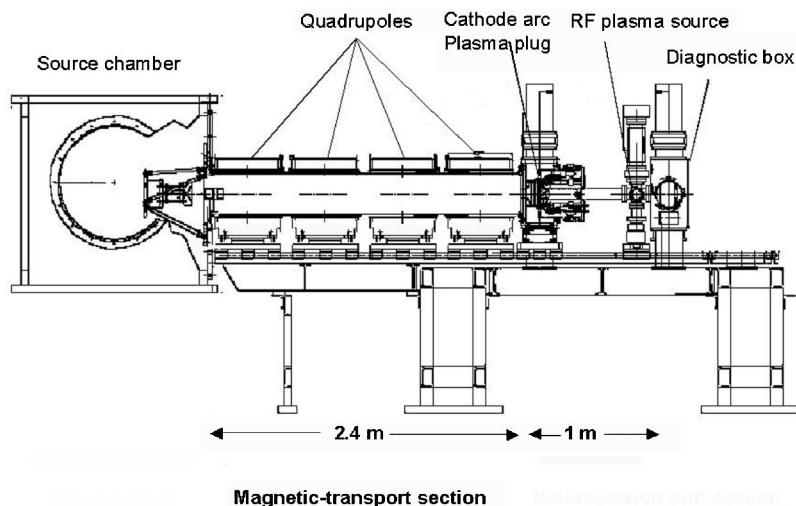


FIG. 1. A sketch of the NTX beam line.

source downstream from the final focus magnet. This plasma acts as an initial source of neutralizing electrons that become entrained downstream with the propagating beam. A second plasma is produced near the focus ( $\sim 1$  m downstream of the final focus magnet) by a pulsed radio frequency source to simulate the effect of the photoionized plasma produced by the heating of the ICF target in the chamber. This volume plasma near the beam waist provides additional neutralization of the beam. Characterization of both plasma sources suggests that a sufficient reservoir of electrons exists to neutralize the NTX beam.

Preliminary simulations of the NTX experiment have been performed utilizing the electromagnetic particle-in-cell (PIC) code LSP.<sup>8,19,20</sup> With the LSP simulations initialized by an idealized particle distribution, or one extracted from the Warp PIC code used to simulate transport through the magnetic quadrupoles,<sup>21</sup> there is a general agreement between the measured focal spot and simulation result.<sup>22</sup> A more careful comparison of density profiles at the nominal focus shows qualitative differences. Notably, the experimental profile has a significant amount of charge in a halo extending past the beam core.<sup>15</sup> This feature is absent from prior LSP simulations. To determine the effect of this difference, it is essential to initialize the simulation with a more realistic phase-space distribution. To this end the four-dimensional (4D) transverse phase-space of the NTX beam is measured upstream of the plasma sources. The phase-space data are used to initialize a new series of 3D LSP simulations to study the neutralization physics of the NTX experiments and to assess the agreement between experiment and simulation results.

Two previous papers<sup>15,23</sup> have reported on the experimental results from the NTX experiments. The objective of this paper is to provide quantitative comparisons of simulations and data where such is possible, and to provide qualitative insight from theory in cases where the data indicate interesting physical phenomena, but where essential details are either incomplete or not measurable in the NTX environment.

## II. NTX EXPERIMENT

The neutralization section of the NTX experiment follows a series of magnetic quadrupoles which direct the beam to a focus  $\sim 1$  m downstream. The localized plasma plug is created outside the quadrupole fringe fields with a sufficient density to neutralize the ion beam (typically  $n_p/Zn_b \gg 1$ , where  $n_p$  and  $n_b$  are the plasma and beam densities, respectively). As the initially unneutralized ions pass through and exit the plug, plasma electrons are accelerated by the ion space charge up to the ion velocity and propagate along with the beam providing charge and current neutralization. To maintain a quasineutral plug region, the plasma should be in contact with a conducting boundary or large plasma region that can resupply electrons.

The volume plasma in the downstream end of the drift section provides additional neutralization to the beam. In contrast to the plasma plug, the plasma neutralization takes place locally. The axial position of the volume plasma is placed strategically in the ion trajectory to provide maximum spot size reduction, and was determined from preliminary LSP runs. The spot size reduction with the addition of the volume plasma was predicted before the experimental results were obtained.

### A. The NTX beam line

The beam line consists of (a) an ion beam injector, (b) four quadrupole magnets, and (c) a 1 m long final focus drift section equipped with a cathode arc plasma plug, rf plasma source, and diagnostics. Figure 1 shows a sketch of the NTX beam line.

The  $K^+$  beam is produced within the source chamber by a hot-plate<sup>24</sup> alumino-silicate source. Pulsed power is provided by a Marx generator and a crowbar switch.<sup>25</sup> This Marx generator produces a pulse with 0.5–1  $\mu$ s rise time and a 6  $\mu$ s “flat-top.” A smooth uniform bright beam profile is generated by high source temperature, smooth source surface, and beam aperturing. The use of variable diameter apertures provides the experimental “knob” to vary the beam

perveance. In addition, the aperture increases the beam brightness by removing the diffuse beam edge.

The beam is transported through a 2.4 m long magnetic section using four pulsed quadrupoles as shown in Fig. 1. The beam pipe radius, the quadrupole length, and quadrupole-to-quadrupole spacing are 14.9 cm, 46.50 cm, and 6 cm, respectively. The field gradient and maximum field of the magnets are calculated to be 2-5 T/m and 0.6 T, respectively, with a current range of 3.3 to 8.2 kA.<sup>26</sup> An electron trap, 7.5 cm in radius, is located at the downstream end of the beam line, 10.2 cm from the last quadrupole lattice. A nominal negative 7 kV voltage is used across this trap to prevent upstream motion of electrons.

The final section of the beam line is known as the neutralized drift section, consisting of a cathode arc plasma plug and rf plasma source. This section is 1 m long and beam diagnostics are installed at the end of the drift section to measure unneutralized and neutralized beams.

A fully ionized Al plasma, produced from a cathodic arc referred to as the metal vapor vacuum arc (MEVVA) ion source, constitutes the plasma plug in the NTX experiment. Metal plasma is generated at cathode spots, and expands rapidly, with ions attaining supersonic velocity of about  $1.5 \times 10^4$  m/s. The streaming metal plasma is injected in a curved solenoid (plasma filter) to remove any liquid or solid debris particles that are produced at cathode spots, as well as neutral metal atoms. The arc current, and, thus, plasma density, can be selected and tuned by the charging voltage of the pulse forming network (PFN). For symmetry reasons, two arc sources produce plasma in such a way that the two plasma streams enter the ion beam region from opposite directions. This MEVVA plasma plug was characterized using a Scientific Systems Langmuir probe, and aluminum plasma density was measured as a function of space and PFN charging voltage. Using the ion saturation current from the measured I-V characteristics and making simplifying assumptions about the aluminum plasma allows us to estimate the plasma density. The measurements show that the plasma density along the axis is peaked at a value of  $10^{11}$  cm<sup>-3</sup> at the location of the pair of entry ports where the plasma enters the beam line and drops off over a distance of a few cm.

The volume plasma is produced from a rf pulsed plasma source which has a six-way cross at the center of its design. The plasma drifts into the center of the cross and intersects the propagating ion beam. The source operates by applying a puff of Ar gas and a pulse of rf power to the antenna. The potential advantages of pulsed operation are that it can easily operate at high peak rf power levels, and the amount of gas can be limited. The plasma density and the neutral gas pressure are issues primarily during the 10  $\mu$ s the ion beam passes through the plasma. Plasma parameters and neutral gas pressure are dynamic quantities and have been measured as a function of time in order to evaluate source operation. The gas valve and the rf power are triggered at the same time ( $t=0$ ). The source is run at a nominal net forward power of  $\sim 3.5$  kW. Before  $t=3.75$  ms, the plasma density is less than the sensitivity of the Langmuir probe ( $\sim 10^7$  cm<sup>-3</sup>), and the neutral pressure is below the sensitivity of the dynamic pressure measurement ( $10^{-6}$  Torr). At  $t=3.75$  ms the electron

density is  $10^{11}$  cm<sup>-3</sup> and the neutral pressure is still low at a few times  $10^{-6}$  Torr. The short ion beam pulse travels through the volume plasma at these conditions.

Several diagnostics have been used to characterize the ion beam. The primary diagnostics for this experiment consist of (1) a Faraday cup, (2) a slit/slit cup, and (3) a scintillator with a gated camera system. The Faraday cup and the slit cup each consist of a collector and a guard ring (grid) with bias voltages that are controlled to collect beam ions only. In addition, we can also monitor currents flowing through the aperture plate and each of the two electron traps. The removable Faraday cup is inserted into the NTX beam line at the exit of the injector and at the end of the magnetic lattices to measure total beam current. The slit/slit cup arrangement is used to measure the line-integrated beam profile (with slit cup only) and emittance (with slit and slit cup) at the same locations. The beam profile is measured optically using a glass or ceramic (96% alumina) scintillator with an associated camera. Charge neutralization of this scintillator is provided by a high-transparency (80%–90% transmission) metallic mesh placed on or near the surface of the scintillator. By applying a negative bias to the mesh, stray external electrons are decelerated and deflected away from the scintillator, limiting their contribution to the optical image to negligible levels. Time resolved beam-induced images on the scintillator screen are captured with a Roper Scientific gated intensified charge-coupled device camera viewing the scintillator through a vacuum window, and images are processed using the public-domain program IMAGEJ. These images are the primary diagnostic used in the analysis for this report. Typical shot-to-shot uncertainty in the data is  $\pm 10\%$ .

The mapping of the 4D phase-space distribution is accomplished over many shots by a scintillator-based imaging technique.<sup>15,27,28</sup> The phase-space distribution  $F(x, y, x', y')$  is measured over multiple shots of the repeatable NTX beam. The beam cross section is scanned just downstream of the final focus magnet by a movable pinhole. The pinhole position specifies coordinates  $x$  and  $y$ . The transmitted beamlet with negligible space charge travels on an effectively ballistic trajectory to the nominal NTX focus where it strikes the scintillator plate. The scintillator image allows extraction of  $x'$  and  $y'$  for each beamlet. The knowledge of the 4D phase space is essential in order to run more realistic simulations of the beam focusing to a small spot when drifting through neutralizing plasma.

## B. Simulation of experimental setup

LSP is used to simulate the neutralization section of the NTX experiment which extends from the region just outside of the fringe fields of the last set of quadrupole magnets to a target  $\sim 1$  m further downstream. The neutralization of an injected ion beam is studied as it passes through the plasma sources by an electromagnetic 3D simulation in cylindrical coordinates.<sup>29</sup>

In order to provide a realistic simulation of the experiment, it is important to include details of the experimental setup. Besides detailed parametrization of the plasma sources and of the incoming ion beam, we must also include or at

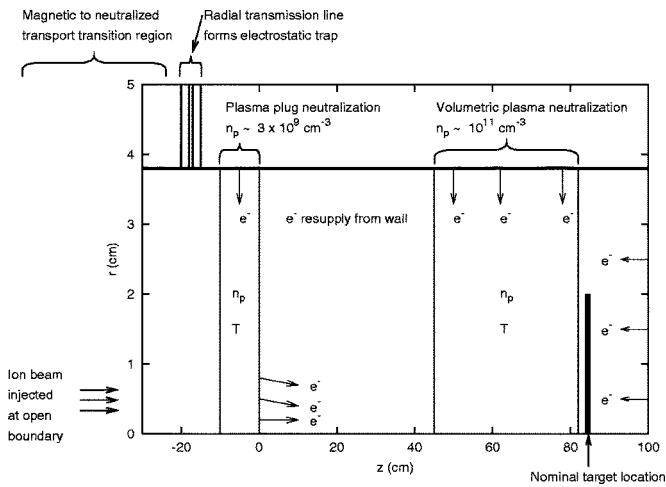


FIG. 2. Schematic of geometry in LSP simulation. Magnetic quadrupoles are located upstream of the start of the simulation.

least assess the effects of the walls, the diagnostic targets, and biased plates used to control unwanted electrons. The details of the experimental setup included in the simulations are shown in Fig. 2.

The simulation space is 130 cm long and 3.8 cm in radius. Particles are injected through an open (Neumann) boundary at  $z = -30$  cm. At initialization a  $C^+$  plasma extends from  $z = -10$  to 0 cm (the experimental plasma ions are  $Al^+$  and  $Al^{+2}$ , but ion dynamics do not play a significant role). The plasma density is cosine weighted with a maximum density of  $3 \times 10^9 \text{ cm}^{-3}$  at  $z = -5$  cm. For numerical reasons (such as the need to resolve the plasma frequency), the simulation density is taken to be an order of magnitude smaller than the actual plug density. The insensitivity of simulation and experimental results to varying plasma density values justifies this approach. The initial electron and ion temperatures are assumed to be a uniform 3 eV. Space-charge-limited emission is allowed where the plasma is in contact with the conducting wall, as well as at the  $z = 100$  cm wall. This is reasonable because the plasma plug extends radially outward from the drift region. At the far endplate, electrons are produced due to ion impact.

A simplified model of the key electron trap just upstream of the MEVVA plasma source is used in the simulation. To prevent electrons from drifting upstream, a biased ring electrode (electron trap) is placed from  $z = -18$  to  $-17$  cm. A radial electromagnetic wave is fed into this port which gives the electrode a negative bias of 5 kV after a several nanoseconds long linear ramp. The volumetric plasma extends from  $z = 45$  to 82 cm with a density profile obtained from the measured densities of the rf source with a maximum density of  $10^{11} \text{ cm}^{-3}$ . Simulation studies again indicate that the neutralization is fairly insensitive to the details of the density distribution. The weak fringe fields of the quadrupole magnet are not included. Preliminary simulations indicate that the effect of these fields on the ion beam in the simulation space is negligible.

There is also an electron trap several centimeters upstream of the scintillator to strip the ion beam of the neutralizing electrons before striking the target. A biased mesh is

placed near the surface of the scintillator to prevent electrons born in ion impact on the surface from streaming back. In general, the effect of these traps on the beam neutralization and spot size was found to be minimal in 2D simulations for  $< 2 \times 10^{-4}$  perveance. Ignoring these traps allows us to place nonintercepting targets at several axial positions in the beam path near focus in a single 3D simulation.

### III. BEAM-PLASMA INTERACTIONS IN NTX

Various experimental results have been previously reported in which different aspects of beam-plasma interactions were observed. In this section, we reexamine these experimental results, and will seek to provide physical insight into the observed phenomena with the help of simulations and theory.

#### A. Partial neutralization in “vacuum transport”

One notable neutralization issue to emerge from the experiment is the partial neutralization of the beam in the absence of the plasma sources. A significant increase in beam spot size for vacuum transport was discovered as the beam pipe was increased in diameter from 7.7 cm to 15 cm.<sup>23</sup> This has been attributed to partial neutralization by secondary electrons produced by grazing collisions of halo ions with the beam pipe. As the pipe diameter is increased these collisions are reduced and secondary electron production is diminished. Electrons created at the wall of a larger beam pipe also spend less time in the path of the beam and are, therefore, less efficient at neutralizing. This effect has been artificially simulated in 2D cylindrical LSP simulations in which the pipe walls are allowed to emit a space-charge-limited supply of electrons from axial positions  $-10$  cm to 1 m. A 24 mA, 256 keV  $K^+$  hard edged beam is injected into a beam pipe with initial radius, divergence, and emittance given by 20 mm, 20 mrad, and  $30\pi$  mm mrad, respectively. Figure 3 shows particle plots (emission electrons are blue, beam ions red) at steady state from the simulations for pipes with radii of 3.8 cm and 7.5 cm. Clearly, the beam radius is larger for the larger pipe. From these results, the effective beam neutralization is estimated by comparing the rms beam radius with an envelope equation in which the effective perveance is fitted to the simulation envelope. This method is described in greater detail in the subsequent sections. Neutralization fractions of 0.34 and 0.10 result from the small and large beam pipes, respectively. The spot size for a 24 mA, 255 keV beam was found experimentally to increase by a factor of two when going to the large pipe.<sup>23</sup> The simulation had a somewhat smaller increase in spot size for the same cases suggesting the possibility of a second electron source. When the plasma sources are on, however, they dominate the neutralization physics.

#### B. Gas effects

It is interesting that the simulations of neutralization for “vacuum transport,” described in the above section, assume copious electron production at the wall, and, yet, it was inadequate to account for the observed level of neutralization

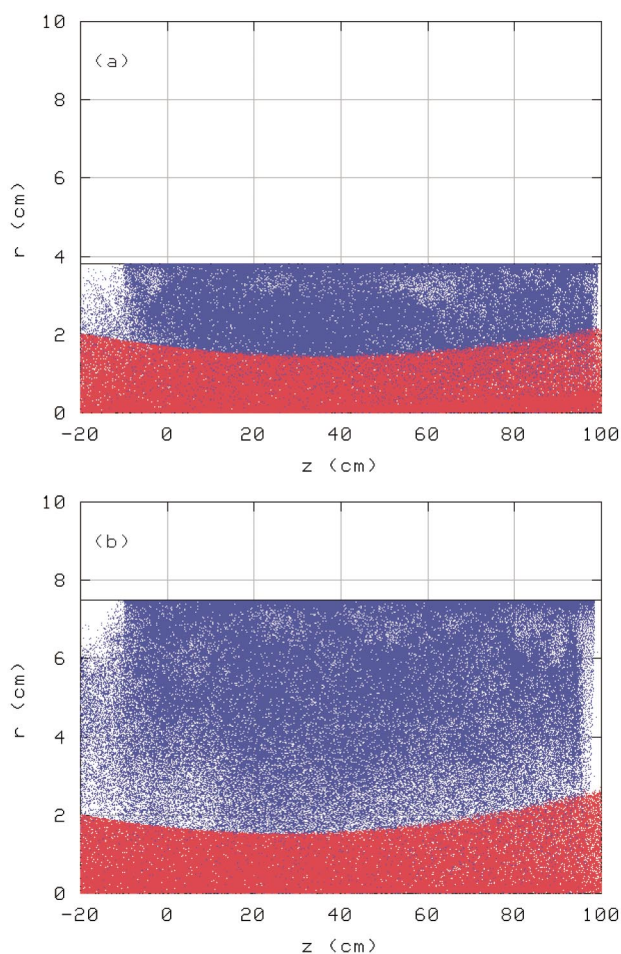


FIG. 3. (Color). Particle plot from a 2D cylindrical LSP simulation for a 24 mA, 20 mm, 20 mrad, 256 keV  $K^+$  beam with emittance of  $30\pi$  mm mrad injected into a beam pipe. Space-charge-limited emission of electrons is allowed on the pipe walls for  $z > -10$  cm. Emitted electrons are shown in blue and beam ions in red. Plot (a) used a 7.5 cm radius pipe, and plot (b) used a 3.8 cm radius pipe.

( $\sim 0.5$  in experiment). A possible explanation is that we have ignored the effects of neutrals emitted from the wall upon ion impact. During the several microseconds of beam time, these neutrals can penetrate into the beam tube and provide additional neutralization by impact ionization. These effects were not modeled, nor is it possible at this point in time to assess the magnitude of this effect since we do not have adequate basic data on neutral production and/or ion-atom cross sections.

In addition to the neutrals produced at the wall, there are also neutrals produced when the MEVVA source and rf plasma source are turned on. The volume or rf plasma source developed at the Princeton Plasma Physics Laboratory (PPPL) (Ref. 30) is intended to model the target plasma created in HIF applications. Operation of the rf plasma source was described in Sec. II A. Time resolved measurements of the neutral Ar pressure and the plasma density show that there is about a 1 ms time window (about 3.75 ms after the rf power is triggered) in which the neutral pressure is of the order of a few times  $10^{-6}$  Torr and the plasma density is about  $10^{11}$   $\text{cm}^{-3}$ . The cross sections for electron capture and

stripping of  $K^+$  ions by Ar atoms are of the order of  $10^{-16}$   $\text{cm}^2$  (Ref. 31) which gives a mean-free path for these processes of the order of  $10^5$  cm. Since the volume plasma extends axially for at most a few tens of centimeters gas effects on the beam can be expected to be negligible at this pressure level. After this initial 1 ms low pressure time window, the neutral gas pressure increases by several orders of magnitude. The timing of the shots is adjusted so that the 10  $\mu\text{s}$  NTX beam passes through the volume plasma region during the low pressure window. The Ar gas is pumped from the beam pipe between shots. The temperature of the volume plasma has been measured to be between 1 and 2 eV on the beam axis. For the MEVVA plug, estimates of neutral pressure and temperature again imply a mean free path of  $\sim 10^5$  cm which is negligible in the 10 cm plug.

### C. Scaling of neutralization with MEVVA plasma density and temperature

The plasma plug is created by a pair of pulsed cathode-arc plasma sources located on each side of the beam axis. The maximum plasma density is found to be of the order of  $10^{11}$   $\text{cm}^{-3}$  and increases as the applied voltage from the power supply is increased (the NTX beam density is only of the order of  $10^8$  as the beam approaches the plug).<sup>15</sup> The density reaches its maximum value axially near the entry ports and is larger near the ports than on the axis. The on-axis density falls by a factor of 10 over an axial distance of about 5 cm. Measurements made by Langmuir probe indicate that the density can vary by about a factor of 4 as the source voltage is increased from 1.5 kV to its maximum value of 2.5 kV. Variations of this order are not expected to significantly affect the neutralization physics, since previous simulations have demonstrated an insensitivity to plug density as long as the plasma density remains significantly larger than the beam density (a factor of 10 is sufficient<sup>22</sup>). Analysis of NTX data at a wide range of plug source voltages verifies that the beam spot size quickly levels off as the voltage is increased. This can be seen in Fig. 4 which plots the  $x$  and  $y$  lineouts of experimental beam images for a 6 mA, 266 keV  $K^+$  beam at the target. With the MEVVA voltage off the beam has a broad core. As the voltage is turned on the core size reduces substantially but varies little over the range from 0.5–2.0 kV. When this analysis is repeated for a 24 mA beam it is found that the beam neutralization begins to deteriorate somewhat for high MEVVA voltages ( $> 2.0$  kV).

Generally, the temperature and density of the plasma plug increase with the applied voltage with temperatures of the order of 3–5 eV.<sup>32</sup> Simulations show little variation in beam neutralization for peak densities above  $5 \times 10^8$   $\text{cm}^{-3}$ , but do indicate that neutralization is adversely affected by plasma temperature when  $T_e$  exceeds the energy required to accelerate the electrons up to the plug velocity. For a 260 keV  $K^+$  beam,  $\frac{1}{2}m_e v_b^2 \sim 4$  eV. One possible explanation for the beam degradation at high MEVVA voltages for the 24 mA beam is that the neutralization deteriorates due to higher plasma temperature. It is not clear why the 6 mA beam does

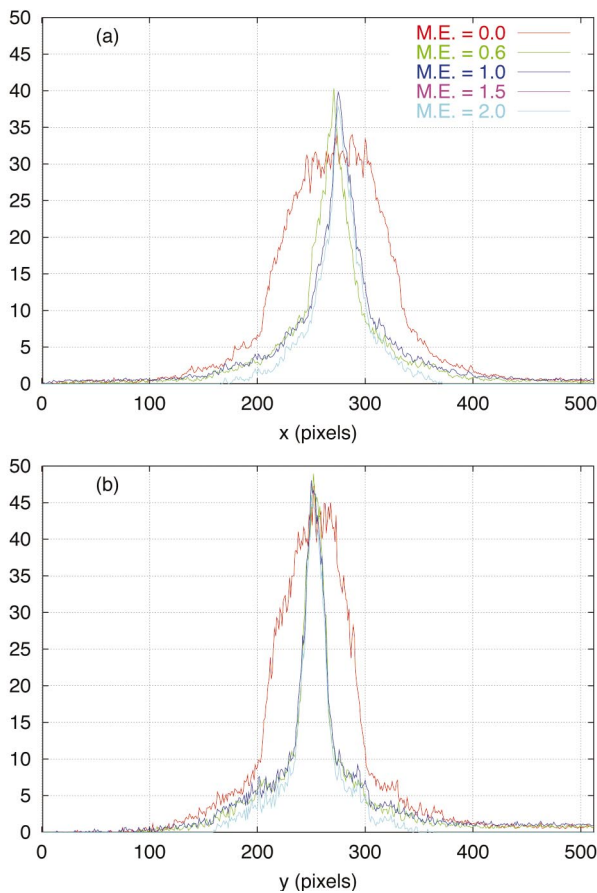


FIG. 4. (Color). Plots of (a)  $x$  and (b)  $y$  lineouts of beam images of a 6 mA, 266 keV  $K^+$  beam at the target location with varying values of MEVVA voltage (kV). The  $x$  and  $y$  axes are in units of image pixels where 1 cm = 89 pixels.

not exhibit similar deterioration. Without a better measurement for plasma plug temperature it is difficult to assess the significance of this effect experimentally.

#### IV. LSP SIMULATION OF THE NTX EXPERIMENT USING EXPERIMENTAL 4D PHASE-SPACE DATA

The 4D phase-space data were obtained as described in Sec. II A. Figure 5 shows the configuration space projection

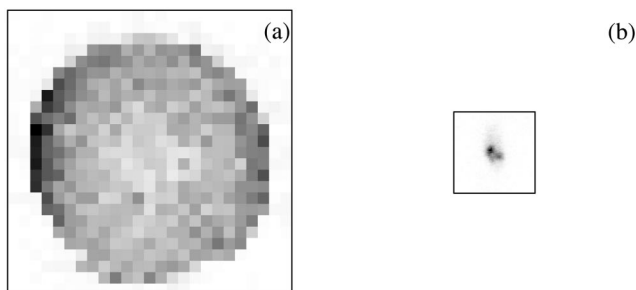


FIG. 5. Configuration space density plot of NTX data for 6 mA, 266 keV  $K^+$  beam at (a) location of pinhole  $z_0$  and (b) location of scintillator  $z_0 + 102$  cm after fully ballistic transport. Both plots are on the same scale. The square in (a) has a length of 35 mm and illustrates the area covered by the pinhole. The square shown in (b) illustrates the scintillator area and has a length of 10 mm.

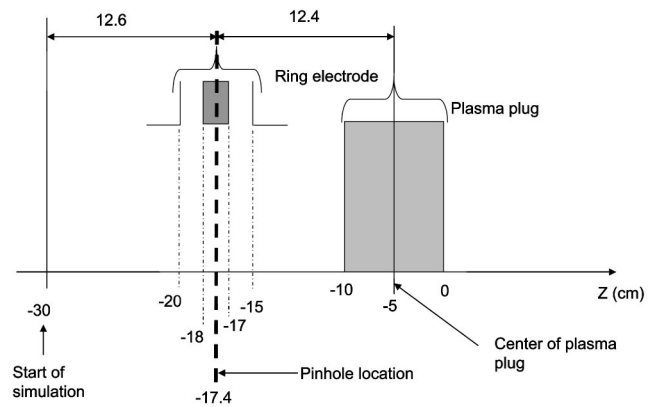


FIG. 6. Closeup of geometry used in LSP simulation. Note that the 4D phase-space pinhole is in the electrostatic trap region. Magnetic quadrupoles are located upstream of the start of the simulation and the volume plasma is downstream from  $z=45$  to 82 cm.

of the 4D phase-space data at  $z_0$  for a 6 mA, 266 keV  $K^+$  beam, and the same beam data when pushed ballistically to  $z_0 + 102$  cm. This figure shows a spot size of the order of 1 mm at the nominal target for perfect neutralization. Table I gives the beam envelope parameters calculated from the same data.

Initial ion beam PIC macroparticles for the simulation need to be sampled from the experimental phase-space data. This is done by a Monte Carlo method which is discussed in detail in Appendix A. The sampled particles are then injected into the simulation at an open boundary at the pinhole location.

Figure 6 shows that the position of the pinhole used in the 4D phase-space measurement is in the region of the ring electrode. This electrode serves as an electrostatic trap to keep plasma plug electrons from drifting upstream. The measured phase-space data are obtained in the absence of plasma, but for the full simulation including the plasma plug it is possible for energetic electrons to drift upstream towards the initial pinhole location due to the space-charge force of the incoming beam head. For this reason it is necessary to transport the initial distribution back upstream prior to starting the simulation. Using the LSP simulation coordinates, the pinhole is located at  $z = -17.4$  cm. The simulation is set up to start at  $z = -30$  cm. This requires running the particles at the pinhole location backwards for 12.6 cm with full space charge. To run the particles backwards, each particle has the sign of its velocity reversed. The particles are then extracted at a plane 12.6 cm upstream of the pinhole. These extracted particles then have their velocities flipped in sign again and are launched into a forward simulation which starts at  $z = -30$  cm. The beam rms values for backwards propagation were compared to envelope equation solutions [Eq. (A6) of Appendix A with an unneutralized perveance of  $K = 1.77 \times 10^{-4}$  for the 6 mA, 266 keV beam] with good agreement.

#### V. COMPARISON OF EXPERIMENTAL RESULTS AND LSP SIMULATION USING 4D PHASE-SPACE DATA

The full 3D plasma simulations are performed in cylindrical coordinates with eight azimuthal spokes. A nonuniform grid is used in the  $r$  and  $z$  coordinate directions to keep

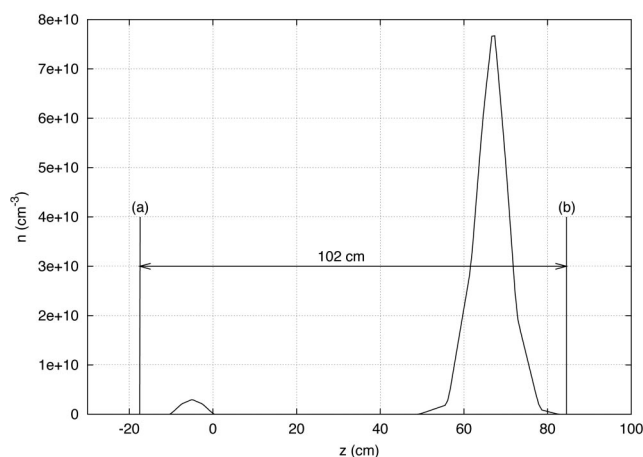


FIG. 7. On-axis density profile of plasma plug (centered at  $z=-5$  cm) and volume plasma (centered at  $z=64$  cm) at  $t\sim 0$ . Vertical lines labeled (a) and (b) denote the axial positions of the pinhole and nominal target, respectively.

the number of grid points from getting prohibitively large. Near the axis  $\Delta r\sim 1$  mm, while  $\Delta z\sim 4$  mm at the upstream open boundary, and  $\sim 1$  cm at the downstream conducting wall. A fully electromagnetic noniterative implicit field solver is used to perform the simulations.<sup>29</sup>

Figure 7 shows the initial on-axis density of the plasma plug and volume plasma. There is no initial transverse variation in the plasma density. The figure also shows the position of the pinhole and nominal target with respect to the plasma. Note that the ion beam must travel about 7.5 cm from the pinhole to the initial edge of the plasma plug. Of course, some electrons from the plug may drift upstream before being stopped by the electrostatic trap. Such electrons will pre-neutralize the beam before it approaches the edge of the plug. All plasma species are initialized with a temperature of 3 eV. All wall emitted electrons are injected into the simulation with the same 3 eV temperature.

The required time step for the simulation is  $\Delta t\sim 0.01$  ns. This constraint is due to a Courant-like condition at the open boundary. For a simulation length of 130 cm for a 266 keV beam, it is necessary to run up to about 1300 ns to reach a steady-state condition. Simulations were performed on a Linux cluster with  $\sim 2.5$  GHz processors with  $\sim 1$  GB of random access memory. Simulations using four processors had run times of the order of two to three days.

Figure 8 shows a particle snapshot at steady state for a simulation with plasma plug and volume plasma present and illustrates the simulation space. In Fig. 9, particle plots are shown again at steady state. In this case the volume plasma is not present and the beam ion and plasma electron macroparticles are plotted separately. It is evident that the plug electrons are entrained by the ion beam. Note also that the left hand edge of the plug stays well localized at  $z=-10$  cm. This means that the ion beam will have to propagate the  $\sim 7.5$  cm from the pinhole location (where the initial phase-space data were acquired) to the leading edge of the plasma plug with negligible neutralization. The effect of this distance on the beam envelope is seen in Fig. 10. This figure shows the  $x$  and  $y$  rms values of the beam as a function of  $z$ , as calculated from particle transverse moments in LSP simu-

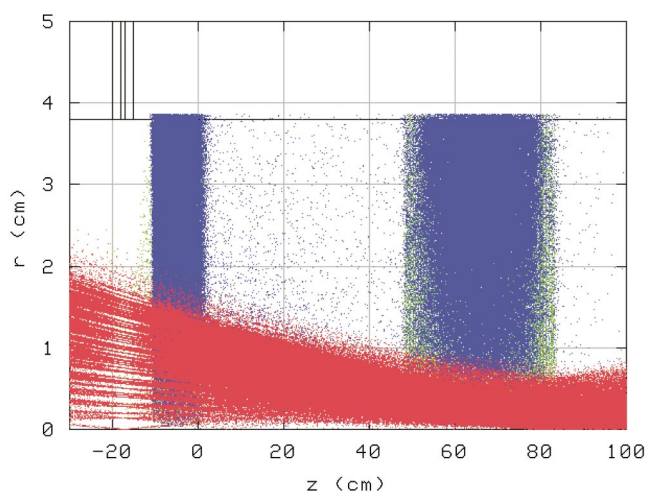


FIG. 8. (Color). Particle plot of simulation of 6 mA, 266 keV  $K^+$  beam with plasma plug and volume plasma at steady state ( $t\sim 1400$  ns). Beam ions are shown in red, plasma ions in green, and electrons in blue. Note that particles with all azimuthal angle values are plotted.

lations. The pinhole location in this figure is  $z=-17.4$  cm with the leading edge of the plasma plug at  $z=-10$  cm. The simulation data labeled (a) shows the plots of beam  $x$  and  $y$  rms values as a function of  $z$  for a perfectly neutralized beam starting from the pinhole. The data labeled (b) are the result of a simulation of a beam which is fully neutralized only after the leading edge of the plasma plug is reached. That is, the beam must travel for 7.5 cm with its full space charge. In the LSP runs, full neutralization is simulated by shutting off

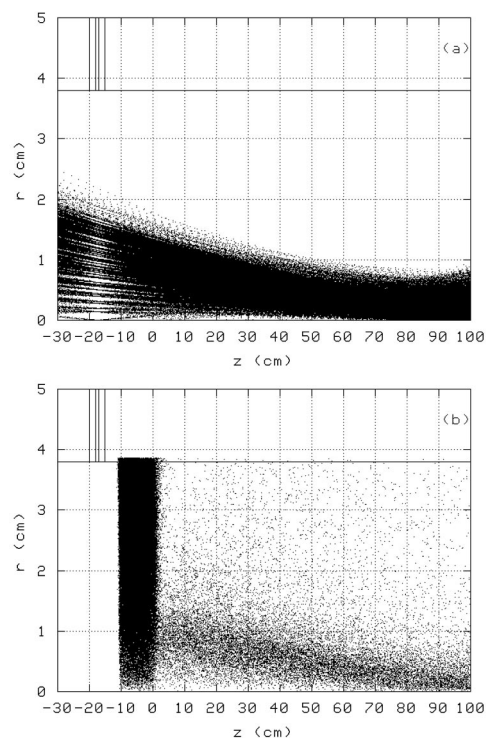


FIG. 9. Particle plot of simulation of 6 mA, 266 keV  $K^+$  beam with plasma plug only at steady state ( $t\sim 1400$  ns). The plots show (a) ion beam macroparticles and (b) plasma plug electron macroparticles.

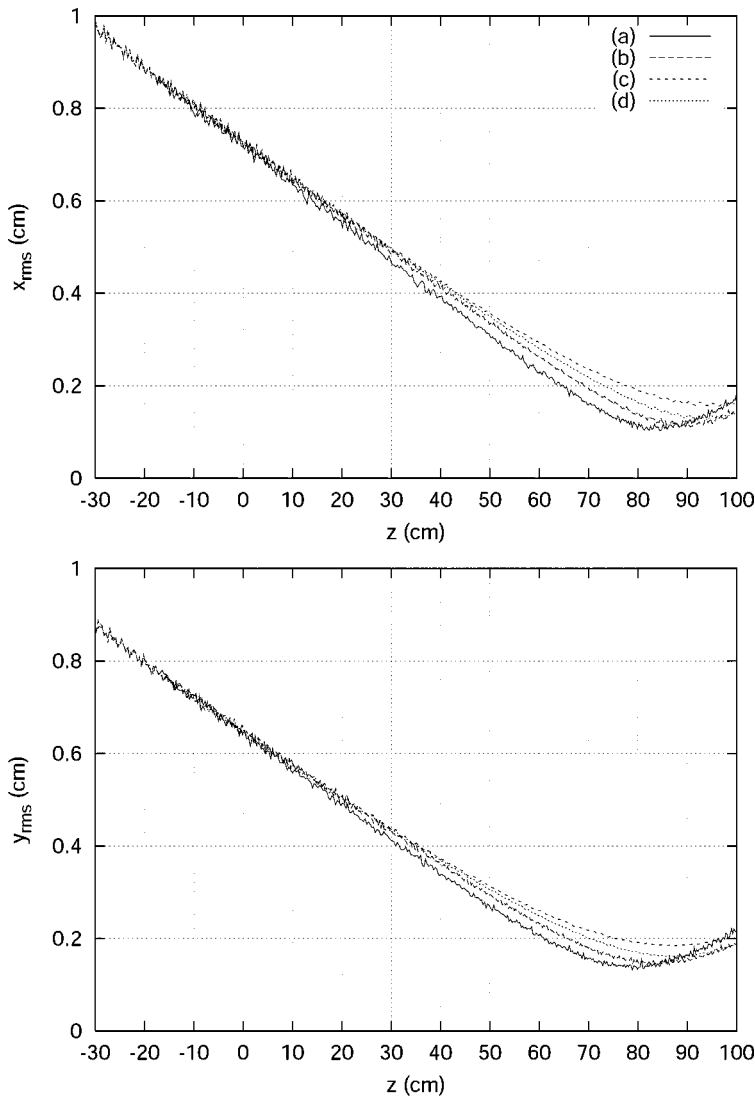


FIG. 10. Plots of beam  $x$  and  $y$  rms values as a function of  $z$  for a 6 mA, 266 keV  $K^+$  beam with (a) perfect neutralization for  $z \geq -17.4$  cm (pinhole location), (b) perfect neutralization for  $z \geq -10$ , (c) plasma plug only present, and (d) plug and volume plasma present. All results are calculated from transverse particle moments of LSP simulations at steady state. The Lorentz forces on the particles are neglected in the appropriate axial regions of simulations (a) and (b).

Lorentz forces on the PIC macroparticles. As seen in the figure, the case in which the beam is neutralized only after reaching the plasma plug focuses a few centimeters farther downstream and has a slightly larger spot size at the minimum than the fully neutralized case.

Also shown in the same figure are the rms values for full LSP simulations with (c) the plasma plug only, and with (d) the plug and volume plasma both present. Comparison of cases (c) and (d) demonstrates that the addition of the volume plasma enhances the neutralization considerably. To estimate the neutralization fraction  $f$  the LSP results for  $x$  and  $y$  rms beam values are compared to solutions to the envelope equations. Equations (A6) of Appendix A are solved with the initial conditions of Table I by taking a simple axial dependence for the perveance. A constant neutralization fraction is taken for the region downstream of the plasma plug ( $z \geq -10$  cm) while the full perveance is used upstream of the plug. Figure 11 shows that this simple neutralization model is in good agreement with  $f=0.81$  for the plasma plug only. Repeating this procedure with the volume plasma present we find the neutralization fraction increases to 0.92.

In Fig. 12, 2D density plots of the ion beam fluence (time-integrated current density) through the nominal target

plane ( $z=84.6$  cm) are plotted for both measured data from the NTX experiment and LSP simulations. The measured data come from scintillator images at the target (except for the fully neutralized case in which data are obtained by ballistically pushing the 4D phase-space data to the target location). The simulation fluence data are acquired by tracking the PIC particles which cross the target plane. The fluence data are

TABLE I. Calculation of transverse moments from 4D phase-space data for a 6 mA, 266 keV  $K^+$  beam. Values at  $z_o+102$  cm are calculated after performing the transformations of Eq. (A3) in Appendix A which assume perfect neutralization. Emittance values are unnormalized  $4 \times$  rms (see, e.g., Ref. 34).

	$z_o$ (cm)	$z_o+102$ (cm)
$a$ (mm)	17.277	2.198
$b$ (mm)	15.599	2.933
$a'$ (mrad)	-16.735	0.556
$b'$ (mrad)	-15.647	4.756
$\epsilon$ (mm mrad)	38.740	38.740
$\epsilon_x$ (mm mrad)	37.057	37.057
$\epsilon_y$ (mm mrad)	44.514	44.514

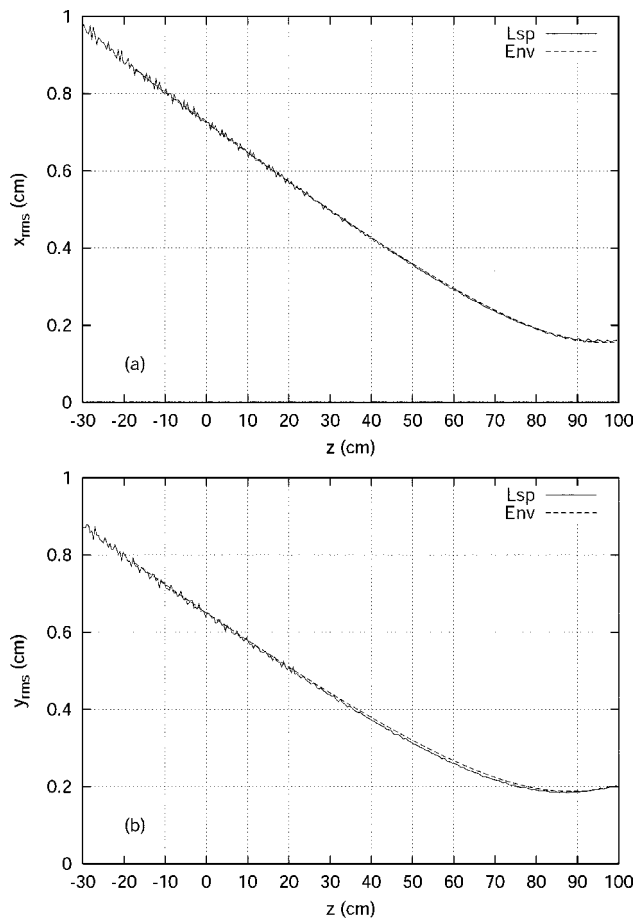


FIG. 11. Plots of beam (a)  $x$  and (b)  $y$  rms values as a function of  $z$  for the 6 mA beam with plasma plug only. The two traces are the LSP results and solutions of the envelope equations with a neutralization fraction of 0.81 in the region downstream of the plasma plug ( $z \geq -10$  cm).

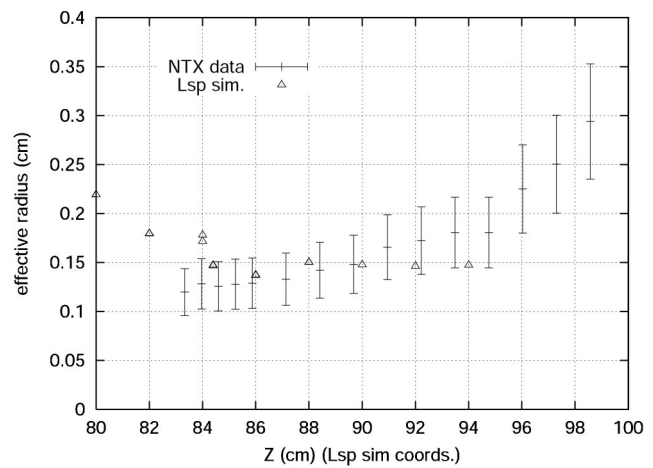


FIG. 13. Comparison of effective beam radius as a function of axial position for simulation and experiment for the 6 mA, 266 keV  $K^+$  beam.

binned on a 2D Cartesian grid, not the cylindrical simulation grid. For each plot in the figure the  $x$  and  $y$  axes span the range from  $-3.5$  to  $3.5$  mm, with the data binned into a  $63 \times 63$  matrix. Each plot in the figure is normalized by the maximum fluence value of that plot. The linear color scale plots blue for zero fluence and red for the maximum normalized fluence of one. The top and bottom rows of the figure, labeled (1) and (2), show the measured and simulated data, respectively. Column (a) is for the case with only the plasma plug present, (b) with plug and volume plasma present, and (c) is for the fully neutralized case. The agreement between the measurement and simulation is good in all cases. In Fig. 13, the simulation and experimental beam radius are com-

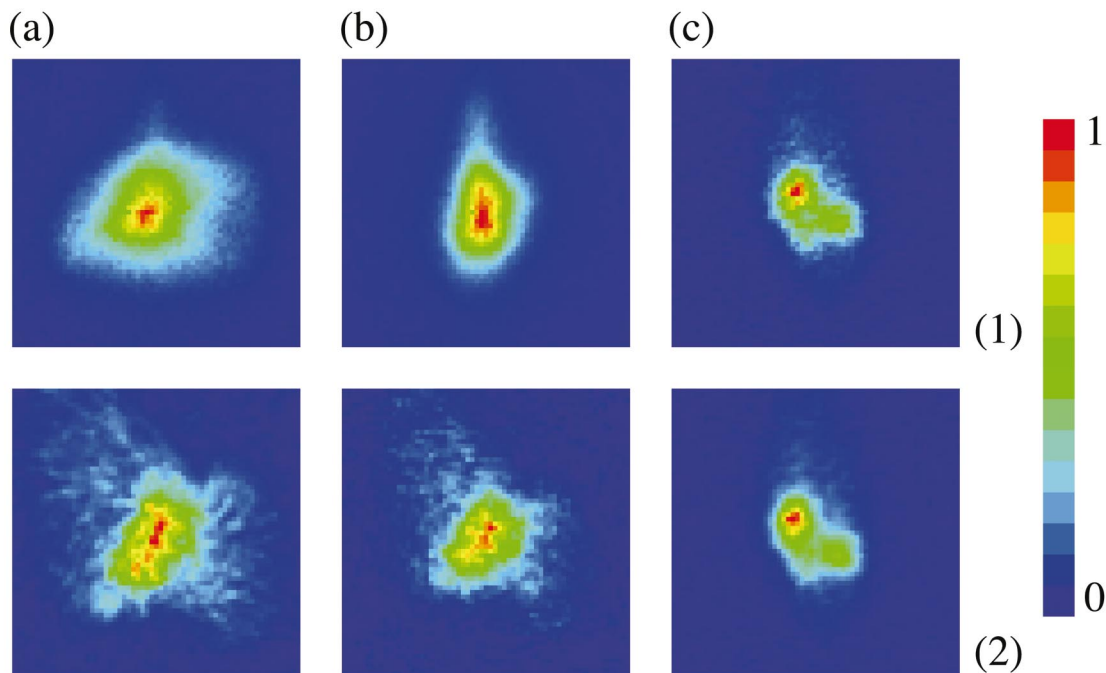


FIG. 12. (Color). Density plots of fluence at the nominal target at steady state for NTX measurements and LSP simulations for the 6 mA, 266 keV  $K^+$  beam. Row (1) gives measured data, and row (2) the simulation results. Column (a) shows the results for the case with only the plasma plug, (b) plasma plug and volume plug, and (c) perfect neutralization from pinhole. In each plot the  $x$  and  $y$  axes cover the range from  $-3.5$  to  $3.5$  mm. The color map is displayed on the right. Note that each plot is individually normalized to its maximum fluence value.

pared over a range of axial positions for the case with only the plasma plug present. The experimental and simulated beam profiles are both well described by a core and diffuse halo. The effective beam radius  $r_e$  is defined as the average distance from the beam centroid to the locus of points with an intensity of  $e^{-1}$  times the maximum. Details concerning the calculation of  $r_e$  are given in Appendix B. The experimental data used in Fig. 13 were taken one week later than the date on which the phase-space data were obtained. (It was only on this later date that images covering a wider axial range were obtained.) The beam image at the target on the later date had roughly the same spot size and features as the data from the week before but was somewhat more elongated in the vertical direction. The elongation in this direction is enhanced as the target is moved downstream. For this reason the experimental data increase at larger  $z$  values, while the simulation data are rather flat. Based on comparisons at the nominal target for data from the two dates, we suspect that some drifting of the beam properties has occurred in the one week interval.

It was noted above in reference to Fig. 10 that the 7.5 cm of unneutralized propagation between the pinhole and the leading edge of the plasma plug has the effect of pushing the focus a few centimeters downstream from the nominal target position of the fully neutralized run. This can also be observed by comparing Fig. 14 with Fig. 15. Figure 14 shows the 2D phase-space projections of ion beam particles at the target location for fully neutralized transport, while Fig. 15 shows the same for simulated transport through the plasma plug and volume plasma. Note that for fully neutralized transport, there is no noticeable slope in  $x-x'$  and  $y-y'$  plots. This is the expected behavior at a beam waist. By contrast, for transport through the plug and volume plasma these same phase-space projections still have a negative slope, which suggests that the beam is still converging at this position.

For the simulation with both the plug and volume plasma, fluence density plots are shown in Fig. 16 at increasing values of axial position. The fluence is plotted at  $z =$  (a) 76, (b) 78, (c) 82, (d) 84, (e) 84.6, (f) 86, (g) 88, (h) 90, and (i) 92 cm. Note that the detailed features of the beam profile vary rapidly with  $z$  and that the fluence plots at (h) 90 and (i) 92 cm assume the approximate shape of the perfectly neutralized result [see Fig. 12, column (c)]. Recall that the fully neutralized result propagates with full neutralization for 102 cm, while the plasma simulation has an extra few centimeters of vacuum propagation. The beam begins to look more like the fully neutralized result when it is allowed to propagate a few centimeters farther downstream.

We find that the simulation results are insensitive to the details of the numerics. The effect of the value of  $N_p$ , the number of particles sampled from the phase-space distribution, on the simulation results has been assessed. When comparing fluence density plots in the target plane at steady state for simulations with the plug and volume plasma present with both  $N_p = 10^4$  and  $10^5$  the overall agreement is good. For the smaller value of  $N_p$  the beam halo appears less uniform and has noticeable pixel effects. This is because fewer distinct particles are sampled from the halo region, and those that are sampled are repeated as the input particles are

wrapped around when the number of injected PIC particles exceeds  $N_p$ , as described in Appendix A. With a larger value of  $N_p$  a greater number of distinct halo particles are sampled and are also wrapped around less frequently, yielding a smoother density distribution, but with only a small effect on the beam spot. The nominal value of  $N_p$  used for this report is  $10^5$ .

As mentioned above, the nominal grid resolution for the simulations in this report have a minimum radial cell size (near the axis) of about 1 mm, and use eight azimuthal spokes, while the fluence density plots have a much higher resolution Cartesian grid. An *ad hoc* justification for the use of a higher resolution grid for the fluence diagnostic is as follows. As in all PIC treatments, the individual particle trajectories are gridless. Only the fields are calculated on the simulation grid. In the case of a highly neutralized beam, the effect of the fields on the particle trajectories will be small compared to the particle initial conditions which are contained in the phase-space information. To ensure that the grid resolution is adequate, several simulations with decreased cell sizes are considered. In addition to the nominal grid, a simulation is performed with double the radial resolution and no change in the azimuthal or axial cell sizes, and a second simulation with 16 azimuthal spokes and no change in the radial or axial cell sizes. Lengthy run times precluded increasing the grid resolution in more than one coordinate direction at a time. We again compare the fluence density plots in the target plane for simulations with plug and volume plasma. The overall fluence plot is found to be largely insensitive to both the doubling of the radial and azimuthal resolution. These calculations suggest that the resolution of the nominal grid is adequate to capture the major features of the neutralization physics. Simulations with increased total particle number (but with a fixed  $N_p$ ) were also performed without a noticeable change in result.

## VI. SCALING OF PLASMA PLUG NEUTRALIZATION

As noted first by Olson, a stationary plug can neutralize the beam only down to a minimum space-charge potential of  $\sim \frac{1}{2}m_e v_b^2$  (the energy required to accelerate the plug electron up to the beam velocity).<sup>33</sup> That is, the neutralization fraction is bounded by the relation:

$$1 - f \geq \frac{\frac{1}{2}m_e v_b^2}{e\phi_{\max}},$$

where  $\phi_{\max}$  is the maximum beam potential, which is, to within a geometric factor of order 1, given by<sup>34</sup>

$$\phi_{\max} \sim \frac{I_b m_e c^2}{I_o e \beta_b},$$

where  $I_o = m_e c^3 / e$  in cgs units. This yields a minimum effective perveance for nonrelativistic ion beams ( $\gamma_b \sim 1$ ),

$$K(1 - f) \sim Z \frac{m_e}{m_b}, \quad (1)$$

which is independent of beam current and energy. The presence of the volume plasma located near the focus can provide additional neutralization below the trapping potential

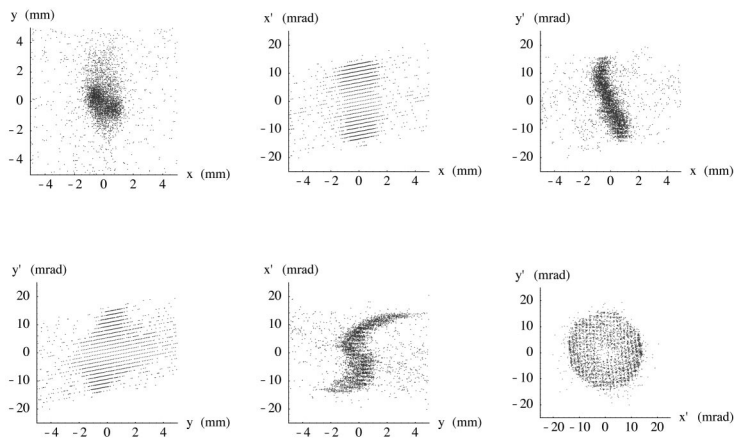


FIG. 14. Two-dimensional phase-space plots of LSP particles from a 6 mA, 266 keV  $K^+$  beam at steady state in a 1 cm axial slice in front of the nominal target (102 cm from pinhole) after fully neutralized transport. Raw particle data are converted from cylindrical to Cartesian coordinates.

because the neutralization is locally limited only by the plasma Debye length.

One motivation for the present study was to verify the plug neutralization scaling of Olson. For the 6 mA beam ( $K=1.77 \times 10^{-4}$ ), the effective neutralization fraction in simulation and experiment was found to be  $f=0.81$ . This gives an effective perveance of  $K(1-f)=3.2 \times 10^{-5}$  which is only about a factor of 2 higher than minimum effective perveance of  $m_e/m_b=1.4 \times 10^{-5}$  for singly stripped K ions.

According to the Olson scaling [Eq. (1)], the minimum effective perveance should be roughly independent of both current and energy. In addition to the 6 mA case examined above, a series of experiments and simulations was performed with a 24 mA beam. Four-dimensional phase-space data were obtained for a 24 mA, 266 keV  $K^+$  beam ( $K=7.09 \times 10^{-4}$ ). Simulations and experimental analysis for the 24 mA case were restricted to the case without the volume plasma.

To estimate the neutralization fraction for this case we again attempted to fit the steady state  $x$  and  $y$  rms values calculated by LSP to solutions of the envelope equations using the initial conditions calculated from the 4D phase-space data. The result is a neutralization fraction of  $f=0.96$ , or an effective perveance of  $K(1-f)=2.8 \times 10^{-5}$  which is very close to the result for the 6 mA simulation. The effective beam radius at the target was found to be 0.24 cm for the

simulation although the radius did decrease to below 2 mm about 10 cm downstream. The experimental data, however, for the higher current case did have a somewhat smaller effective radius of 0.21 cm at the target and was rounder than the somewhat elongated simulation result. The beam spot and shape was, however, observed to be much more sensitive than the 6 mA case to the electron trap voltages. The downstream electron trap, which can affect the results for higher perveance beams, was on for the data considered, but was not simulated. The 24 mA beam was noted above to be more sensitive to the MEVVA voltage. There is also a somewhat limited set of results at 24 mA compared to the 6 mA data (images over a wide axial range were not available). For these reasons it is difficult to assess the cause of the discrepancy in spot size and shape. The experimental results for the high current case are not, however, inconsistent with the Olson scaling result.

## VII. DISCUSSION AND CONCLUSIONS

We have demonstrated that 3D simulations of the neutralization region of the NTX experiment by the PIC code LSP can capture most of the neutralization physics of the beam-plasma interaction. We obtained good qualitative and quantitative agreement with NTX experimental measurement of beam profiles at the target when initializing the simulation

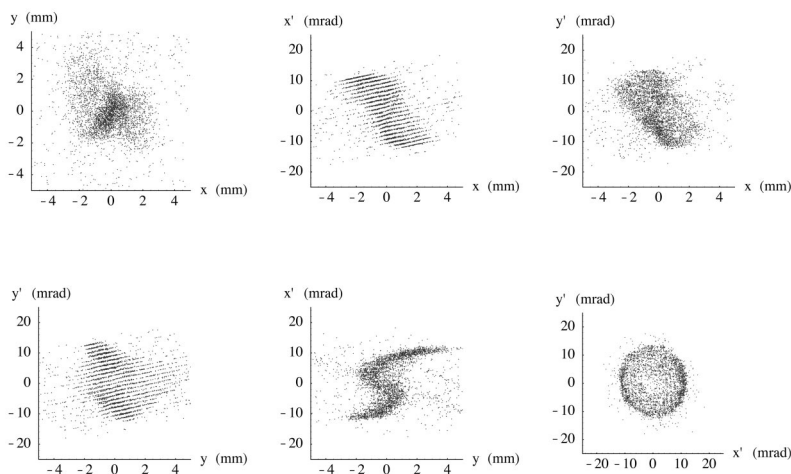


FIG. 15. 2D phase-space plots of LSP particle data for 6 mA, 266 keV  $K^+$  beam transported through the plug and volume plasmas. Includes particles in 1 cm axial slice between  $z=[84.1,85.1]$  cm. Raw data are converted from cylindrical to Cartesian coordinates.

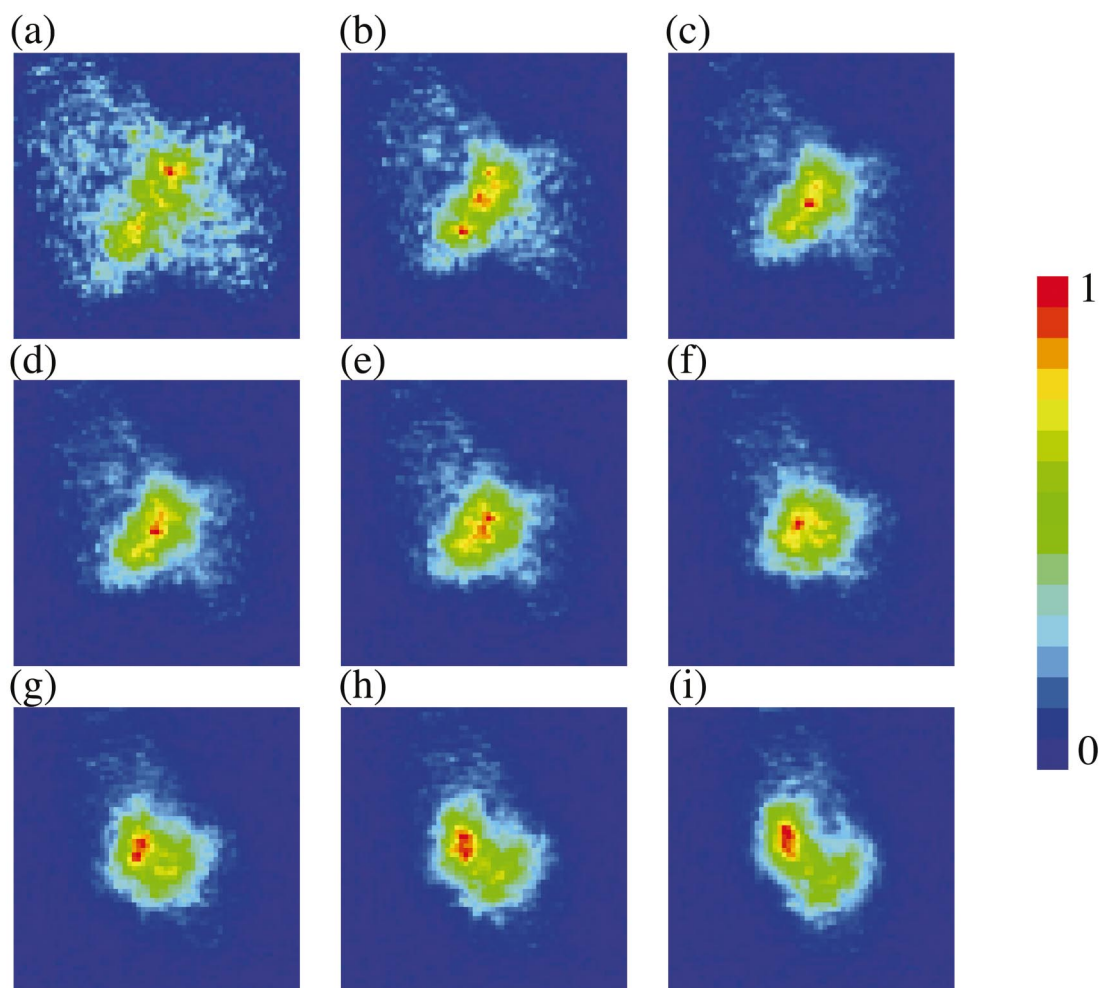


FIG. 16. (Color). Density plots of fluence at steady state for an LSP simulation of 6 mA, 266 keV  $K^+$  beam with plug and volume plasma present at increasing axial positions.  $z =$  (a) 76 cm, (b) 78 cm, (c) 82 cm, (d) 84 cm, (e) 84.6 cm, (f) 86 cm, (g) 88 cm, (h) 90 cm, and (i) 92 cm. In each plot the  $x$  and  $y$  axes cover the range from  $-3.5$  to  $3.5$  mm. The linear color map is displayed on the right. Note that each plot is individually normalized to its maximum fluence value.

with measured 4D phase-space data for a 6 mA beam. The simulations predict measured spot size well and gross features of the beam at the target at this current. Simulations at a higher current of 24 mA were found to be somewhat larger than the best available experimental beam images. The observed strong dependence of the experimental beam spot size on the electron trap voltages for the higher current case could explain the difference, since the downstream electron trap was not simulated.

Simulations at both current values with only the plasma plug present were found to be neutralized down to nearly the minimum trapping potential in agreement with Olson. In practice, the transverse compression of the beam and resulting electron heating degrade the neutralization from its theoretical limit.

The experiment had several sources of uncertainty that can account for much of the differences seen in detailed comparisons with simulation. An experimental shot-to-shot variation of the order of  $\pm 10\%$  is typically observed in the measured spot size. Simulation predictions and measurements show that the plasma plug neutralization is not sensitive to variation in plasma density as long as the plasma

temperature remains  $< 4$  eV. The axial position at which the neutralization effectively begins is defined by the position of the electron trap. The exact position of the rf plasma can have a large effect. Ideally, this plasma source would extend the whole distance from target to plasma plug. Variation in the axial extent of this plasma leads to variation in focal position and spot size.

We have demonstrated the utility of the 4D phase-space reconstruction technique in understanding the neutralization physics. The calculated and measured minimum effective permeance from the plasma plug neutralization and the added neutralization of the volume plasma go a long way in validating the NBT scheme for HIF and HEDP purposes.

#### ACKNOWLEDGMENTS

The authors express their appreciation for useful discussions and support from Grant Logan, Alex Friedman, Christine Celata, David Rose, Igor Kaganovich, and Ron Davidson.

This work was supported by the Director, Office of

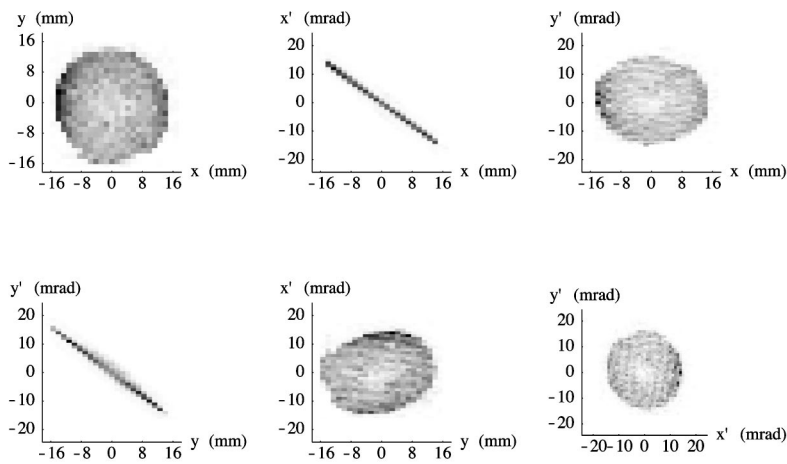


FIG. 17. 2D projections of 4D phase-space data for 6 mA, 266 keV  $K^+$  ion beam at the pinhole location  $z_o$ . The  $x$  and  $y$  coordinate data have 25 bins of width 1.4 mm. The  $x'$  and  $y'$  data have 47 bins of width 1 mrad.

Science, Office of Fusion Energy Sciences, of the U.S. Department of Energy under Contract No. DE-AC03-76SF00098.

#### APPENDIX A: 4D PHASE-SPACE DATA

After some postprocessing of the raw data, the NTX 4D phase-space data at the pinhole location consist of five columns:

$$\{x_i, y_i, x'_i, y'_i, s_i\}, \quad (\text{A1})$$

where

$$i = 1, 2, \dots, N. \quad (\text{A2})$$

The first four columns give the phase-space coordinates of the  $i$ th data point and  $s_i$  gives the corresponding signal strength which is proportional to the intensity of the scintillator flash (signals are given in integer units with the smallest nonzero signal assigned a value of 1). For this report we used 4D phase-space data for a 6 mA, 266 keV and a 24 mA, 256 keV  $K^+$  beam. Figure 17 shows the six 2D projections of the phase space for the 6 mA beam at the pinhole. The  $x$  and  $y$  data have 25 bins of width 1.4 mm. This is also the approximate pinhole size. The  $x'$  and  $y'$  data have been rebinned into 47 bins of width 1 mrad.

Assuming that the beam is perfectly neutralized (i.e., force free) downstream of the pinhole the phase-space data may be trivially transported by the following transformation:

$$x_i(z) = x_i(z_o) + (z - z_o)x'_i(z_o), \quad (\text{A3})$$

$$y_i(z) = y_i(z_o) + (z - z_o)y'_i(z_o),$$

where  $z_o$  is the original pinhole location. Figure 18 plots the 2D projections of the transported phase-space obtained from Eq. (A3) at the nominal focus  $z = z_o + 102$  cm for a fully neutralized beam. This is also the location of the scintillator at which the input data were obtained. The  $x$  and  $y$  coordinate data have 87 bins of width 0.115 mm. The  $x'$  and  $y'$  data have 47 bins of width 1 mrad.

Moments of the distribution can be calculated in the usual way,

$$\langle g(x, y, x', y') \rangle = \frac{\sum_{i=1}^N g(x_i, y_i, x'_i, y'_i) s_i}{\sum_{i=1}^N s_i}, \quad (\text{A4})$$

where  $g$  is an arbitrary function of the transverse phase-space coordinates. The properties of the beam envelope and emit-

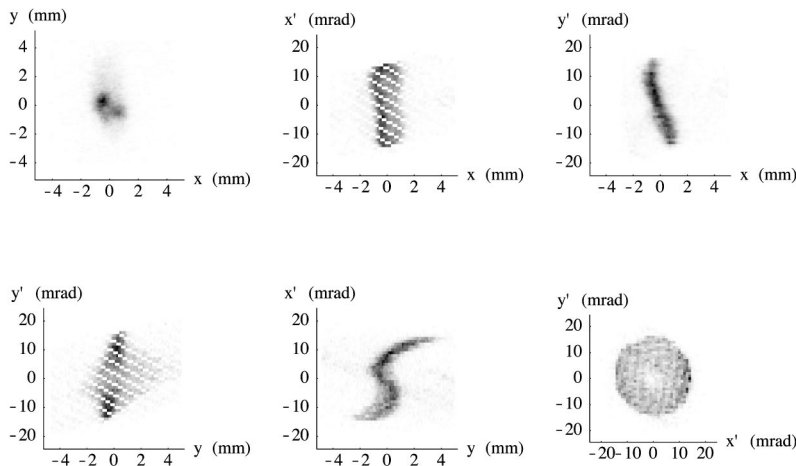


FIG. 18. 2D projections of 4D phase-space data for 6 mA, 266 keV  $K^+$  ion beam at scintillator location  $z_o + 102$  cm. The  $x$  and  $y$  coordinate data have 87 bins of width 0.115 mm. The  $x'$  and  $y'$  data have 47 bins of width 1 mrad.

tance can be calculated from various particle moments. For example, the beam edge radius and divergence in the  $y=0$  plane are given by

$$a = 2\sqrt{\langle x^2 \rangle - \langle x \rangle^2}, \quad (A5)$$

$$a' = \frac{4(\langle xx' \rangle - \langle x \rangle \langle x' \rangle)}{a},$$

with analogous equations for the edge radius and divergence in  $x=0$  plane,  $b$  and  $b'$ . Table I gives the beam envelope parameters calculated from the 4D phase-space data at the pinhole location,  $z_0$ , and when transported by 102 cm with perfect neutralization. The envelope equations for an unrotated elliptically shaped beam are given by

$$a'' - \frac{2K}{a+b} - \frac{\epsilon_x^2}{a^3} = 0, \quad (A6)$$

$$b'' - \frac{2K}{a+b} - \frac{\epsilon_y^2}{b^3} = 0,$$

where the prime denotes a derivative with respect to the axial coordinate. The  $4\times$  rms (unnormalized) emittances are defined by

$$\epsilon_x = 4\sqrt{\langle x^2 \rangle \langle x'^2 \rangle - \langle xx' \rangle^2}, \quad (A7)$$

$$\epsilon_y = 4\sqrt{\langle y^2 \rangle \langle y'^2 \rangle - \langle yy' \rangle^2},$$

and the perveance  $K$  may include a neutralization fraction factor  $(1-f)$ .

To sample PIC macroparticles from the 4D phase-space data the following procedure is used. A discrete probability distribution is constructed from the data in Eq. (A1),

$$P_i = \frac{\sum_{j=1}^i s_j}{\sum_{j=1}^N s_j}. \quad (A8)$$

Note that  $P_0=0$ , and  $P_N=1$ . To select phase-space values for a PIC macroparticle from the probability distribution a random number is chosen over a uniform interval,

$$R \in [0, 1]. \quad (A9)$$

$R$  is then sorted into the appropriate phase-space bin. If

$$P_{i-1} \leq R < P_i, \quad (A10)$$

a particle is created with phase-space coordinates  $x_i, y_i, x'_i$ , and  $y'_i$ . This procedure is repeated until a desired number  $N_p$  of distinct macroparticles has been generated.  $N_p$  was taken to be  $10^5$  for the simulations in this report. All particles chosen in this fashion are given the same charge weight value and the same axial velocity. PIC particles are then injected into the simulation from an open boundary at the pinhole location. Each particle is given a time stamp and particles are injected during the time step in which their time stamp falls. The rate at which ions are injected into the simulation is fixed by the rate of increase of the time stamp. This same

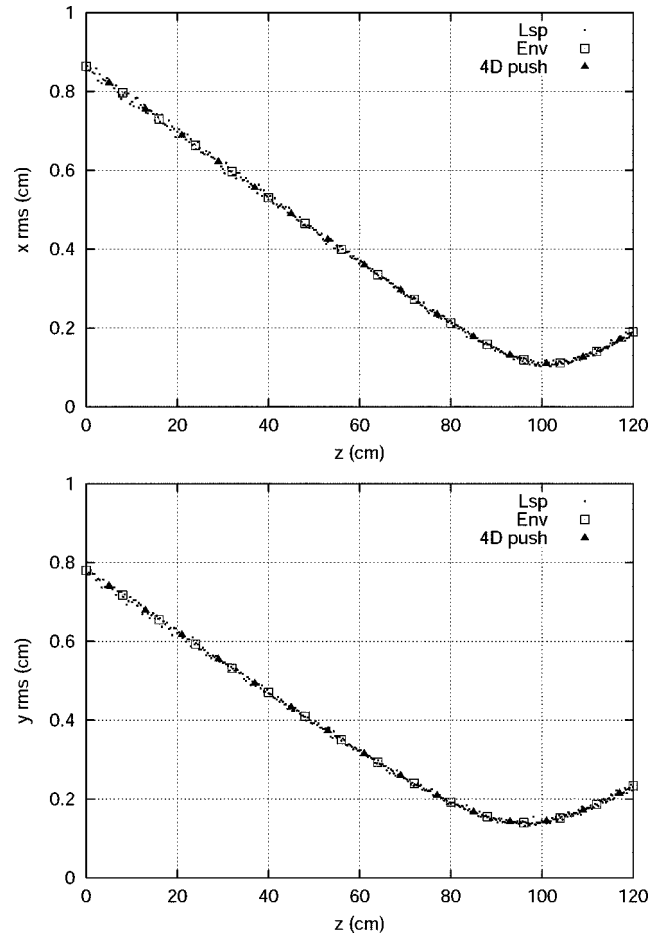


FIG. 19. Plots of beam  $x$  and  $y$  rms values as a function of  $z$  for a perfectly neutralized 6 mA, 266 keV  $K^+$  beam starting from the pinhole. The  $z$  axis has been shifted so that the pinhole is at  $z=0$  cm.

rate and the charge weight value also fix the ion beam current. If the simulation continues long enough such that the number of injected particles reaches a multiple of  $N_p$ , the injection routine wraps around and begins with the first particle again.

To demonstrate that the particle sampling and injection procedure is reasonable, a perfectly neutralized PIC simulation is performed for the 6 mA beam. That is, the PIC particles are pushed with the Lorentz forces artificially shut off. The particles are injected into an open boundary at the pinhole location and allowed to propagate ballistically for about 1 m. The  $x$  and  $y$  rms values for the LSP simulation are plotted in Fig. 19 as a function of  $z$ . The rms values are calculated by taking the transverse moments of the PIC particles in thin axial slices. Also plotted are the solutions of the envelope equations given in Eq. (A6) with perveance  $K=0$  for perfect neutralization, as well as the results of pushing the raw phase-space data as in Eq. (A3). Note that the  $z$  axis has been shifted in the plots so that the pinhole location is at the origin. All three methods give the same results for the rms radii of the beam. Figures 14 and 20 show 2D transverse phase-space projections of LSP particles in a 1 cm axial slice at the pinhole location and at the nominal target location (102 cm downstream of pinhole). Comparison with Figs. 17 and 18 shows that the PIC particles capture and accurately

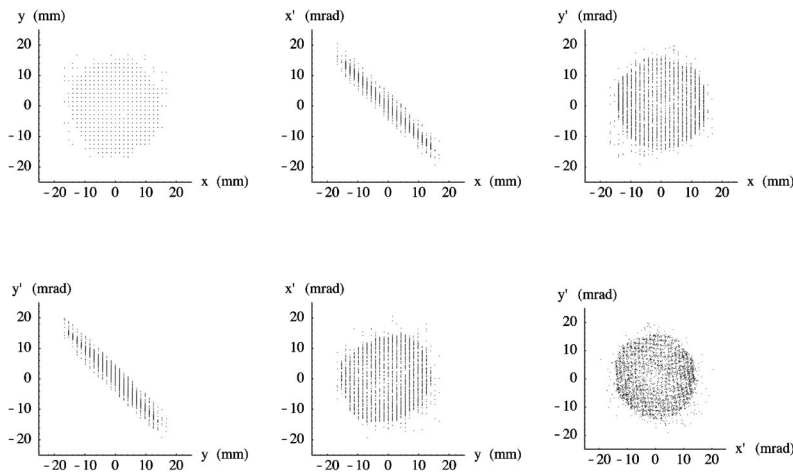


FIG. 20. 2D phase-space plots of LSP particles from a 6 mA, 266 keV  $K^+$  beam at steady state in a 1 cm axial slice in front of the pinhole. Comparison with Fig. 17 shows that the discrete particles capture the phase-space information.

transport the phase-space information for the fully neutralized case.

## APPENDIX B: CALCULATION OF EFFECTIVE BEAM RADIUS

Determining a valid figure of merit for the beam size from scintillator images is complicated by several factors. The raw data tend to have a significant amount of pixel noise as well as background. Calculation of the rms beam radius from the raw moments of the data is very sensitive to the manner in which the background is removed from the image as well as to the tails of the distribution. The partially neutralized beams considered tend to have a relatively small core along with a large halo, with the latter dominating the rms value. For these reasons the rms beam radius (which is very useful for purposes of comparison to the envelope equation) as calculated from the image data tends not to be a good figure of merit for the beam size. In this appendix we describe a procedure for calculating an effective beam radius. Although this method was devised for analyzing the NTX scintillator images, simulation results were processed in the same manner, allowing for a direct comparison of beam sizes.

We have chosen to model the beam intensity from the image data with a weighted sum of 2D Gaussians,

$$I(x,y) = \sum_i n_i e^{-[(x-x_i)/a_i]^2 - [(y-y_i)/b_i]^2} + \text{background}, \quad (\text{B1})$$

where the parameters  $a_i, b_i, x_i, y_i$ , and  $n_i$  are determined by fitting to the image data after removal of the background. It is usually sufficient to model the background pixel values by a plane and to subtract it manually from the image. For the remainder of this treatment it is assumed that the background has been removed. By fitting the raw data to smooth analytical functions the effect of pixel noise on beam statistics is minimized.

Rather than do nonlinear curve fitting of a large 2D data set it is convenient to fit the 1D lineouts

$$I_x(x) = \int I(x,y) dy,$$

$$I_y(y) = \int I(x,y) dx.$$

The lineouts, by virtue of being integrated in one coordinate direction, are also generally less noisy than the 2D data. If the lineouts are normalized to integrate to one, the analytical lineouts are given by

$$I_x(x) = \sqrt{\pi} \sum_i \frac{\alpha_i}{a_i} e^{-[(x-x_i)/a_i]^2},$$

$$I_y(y) = \sqrt{\pi} \sum_i \frac{\alpha_i}{b_i} e^{-[(y-y_i)/b_i]^2},$$

where

$$\alpha_i = \frac{n_i a_i b_i}{M},$$

and  $M$  is the total integrated signal. The lineouts obtained from the image data are then fitted to the analytical forms above by standard techniques for nonlinear curve fitting.

For a beam that can be well characterized by a core and halo it is natural to fit the data to two Gaussian distributions. As a further simplification it is assumed that both Gaussians are centered at the same location ( $x_1=x_2, y_1=y_2$ ). In this case the maximum intensity of the fitted analytical function is located at the center of mass,  $x_1, y_1$ . In the center of mass coordinate system the equation of the curve, which has an intensity  $1/e$  of the maximum, is given by the equation

$$(n_1 + n_2)e^{-1} = n_1 e^{-(x/a_1)^2 - (y/b_1)^2} + n_2 e^{-(x/a_2)^2 - (y/b_2)^2}.$$

Converting to circular polar coordinates, this equation can be solved numerically for  $r(\theta)$ . The effective  $1/e$  beam radius is then given by averaging over the angle  $\theta$ :

$$r_e = \frac{1}{2\pi} \int_0^{2\pi} d\theta r(\theta).$$

Note that the fitted parameters are obtained from the lineout data only and not the general 2D image data. Since the two lineout functions constitute a dramatic reduction of

the original data set it is important to verify after the fact that the fitted 2D intensity function does indeed approximate the original image data well.

- <sup>1</sup>N. Barboza, *Fusion Eng. Des.* **32-33**, 453 (1996).
- <sup>2</sup>D. Callahan, *Fusion Eng. Des.* **32-33**, 441 (1996).
- <sup>3</sup>B. Logan and D. Callahan, *Nucl. Instrum. Methods Phys. Res. A* **415**, 468 (1998).
- <sup>4</sup>W. Sharp *et al.*, *Bull. Am. Phys. Soc.* **44**, 201 (1999).
- <sup>5</sup>J. L. Vay, *13th International Conference on Laser Interaction and Related Plasma Phenomena, Monterey 1997*, edited by G. Miley and E. Campbell, AIP Conf. Proc. No. 406 (AIP, Woodburg, NY, 1997), p. 267.
- <sup>6</sup>I. Kaganovich, G. Shvets, E. Startsev, and R. Davison, *Phys. Plasmas* **8**, 4180 (2001).
- <sup>7</sup>D. Rose, D. Welch, B. Oliver, R. Clark, W. Sharp, and A. Friedman, *Nucl. Instrum. Methods Phys. Res. A* **464**, 299 (2001).
- <sup>8</sup>D. Welch, D. Rose, B. Oliver, R. Clark, W. Sharp, and A. Friedman, *Nucl. Instrum. Methods Phys. Res. A* **464**, 134 (2001).
- <sup>9</sup>R. Bangerter, *Fusion Eng. Des.* **32-33**, 27 (1996).
- <sup>10</sup>S. Yu, W. Meier, R. Abbott, J. Barnard, T. Brown, D. Callahan, C. Debonnel, P. Heitzenroeder, J. Latkowski, B. Logan *et al.*, *Fusion Sci. Technol.* **44**, 266 (2003).
- <sup>11</sup>L. Grisham, *Phys. Plasmas* **11**, 5727 (2004).
- <sup>12</sup>C. Olson, *Nucl. Instrum. Methods Phys. Res. A* **464**, 118 (2001).
- <sup>13</sup>S. Yu, A. Anders, F. Bieniosek, S. Eylon, E. Henestroza, P. Roy, D. Shuman, W. Waldron, W. Sharp, D. Rose *et al.*, *Proceedings of the 2003 Particle Accelerator Conference, 2003*.
- <sup>14</sup>E. Henestroza, A. Anders, S. Eylon, P. Roy, W. Sharp, S. Yu, D. Rose, D. Welch, P. Efthimion, and E. Gilson, *Proceedings of the 2003 Particle Accelerator Conference, 2003*.
- <sup>15</sup>E. Henestroza, S. Eylon, P. Roy, S. Yu, A. Anders, F. Bieniosek, W. Greenway, B. Logan, R. MacGill, D. Shuman *et al.*, *Phys. Rev. ST Accel. Beams* **7**, 083501 (2004) (<http://prst-ab.aps.org/>).
- <sup>16</sup>D. Welch, D. Rose, W. Sharp, and S. Yu, *Laser Part. Beams* **20**, 621 (2003).
- <sup>17</sup>S. MacLaren, M. de Hoon, A. Faltens, W. Ghiorso, and P. Seidl, *Nucl. Instrum. Methods Phys. Res. A* **464**, 126 (2001).
- <sup>18</sup>D. Welch, D. Rose, S. Yu, and C. Olson, *Proceedings of the 2003 Particle Accelerator Conference, 2003*.
- <sup>19</sup>T. Hughes, S. Yu, and R. Clark, *Phys. Rev. ST Accel. Beams* **2**, 110401 (1999) (<http://prst-ab.aps.org/>).
- <sup>20</sup>LSP is a software product of ATK Mission Research (<http://www.mrcabq.com>).
- <sup>21</sup>E. Henestroza, *Third International Conference on Inertial Fusion Sciences and Applications, 2003*.
- <sup>22</sup>D. Welch, D. Rose, S. Yu, and E. Henestroza, *Third International Conference on Inertial Fusion Sciences and Applications, 2003*.
- <sup>23</sup>P. Roy, S. Yu, E. Henestroza, A. Anders, F. Bieniosek, W. Greenway, B. Logan, W. Waldron, D. Vanacek, D. Welch *et al.*, *Phys. Plasmas* **11**, 2890 (2004).
- <sup>24</sup>D. Baca, J. Kwan, and J. Wu, *Proceedings of the 2003 Particle Accelerator Conference, 2003*.
- <sup>25</sup>W. Fawley, T. Garvey, S. Eylon, E. Henestroza, A. Faltens, T. Fessenden, K. Hahn, L. Smith, and D. Grote, *Phys. Plasmas* **4**, 880 (1997).
- <sup>26</sup>D. Shuman, S. Eylon, E. Henestroza, P. Roy, W. Waldron, S. Yu, and T. Houck, *Proceedings of the 2003 Particle Accelerator Conference, 2003*.
- <sup>27</sup>F. Bieniosek, L. Prost, and W. Ghiorso, *Proceedings of the 2003 Particle Accelerator Conference, 2003*.
- <sup>28</sup>A. Friedman, F. Bieniosek, C. Celata, D. Grote, and P. Seidl, *Proceedings of the 2003 Particle Accelerator Conference, 2003*.
- <sup>29</sup>D. Welch, D. Rose, R. Clark, T. Genoni, and T. Hughes, *Implementation of a Non-Iterative Implicit Electromagnetic Field Solver for Dense Plasma Simulation*, presented at the *18th International Conference on Numerical Simulation of Plasmas, Sept. 7-10, 2003*, Falmouth, Massachusetts.
- <sup>30</sup>P. Efthimion, E. Gilson, L. Grisham, P. Kolchin, R. Davison, S. Yu, and B. Logan, *Laser Part. Beams* **21**, 37 (2003).
- <sup>31</sup>H. Lo and W. Fife, *At. Data* **1**, 305 (1970).
- <sup>32</sup>A. Anders, *Phys. Rev. E* **55**, 969 (1997).
- <sup>33</sup>C. Olson, *Heavy Ion Inertial Fusion*, edited by M. Reiser, T. Goodlove, and R. Bangerter, AIP Conf. Proc. No. 152 (AIP, New York, 1986), p. 215.
- <sup>34</sup>M. Reiser, *Theory and Design of Charged Particle Beams* (Wiley, New York, 1994).